IEEE Access
Multidisciplinary | Rapid Review | Open Access Journal

Received 22 September 2022, accepted 7 October 2022, date of publication 13 October 2022, date of current version 20 October 2022.

Digital Object Identifier 10.1109/ACCESS.2022.3214507

RESEARCH ARTICLE

Experimental Assessment of a Magnetic Induction-Based Receiver for Magnetic Communication

JANG-YEOL KIM[1], HYUN JOON LEE[1], JAE-HO LEE[2], JUNG HOON OH[1], AND IN-KUI CHO[1]

[1]Radio & Satellite Research Division, Electronics and Telecommunications Research Institute, Daejeon 34129, South Korea
[2]Department of Electronic Engineering, Kunsan National University, Gunsan 54150, South Korea

Corresponding author: In-Kui Cho (cho303@etri.re.kr)

This work was supported by the Institute of Information & Communications Technology Planning & Evaluation (IITP) grant funded by the Korea government (MSIT) (No.2019–0–00007, Magnetic Field Communication Technology Based on 10pT Class Magnetic Field for Middle and Long Range).

ABSTRACT This paper presents the topology of a novel approach to magnetic communication using a differential magnetic induction (MI)-based receiver and a differential MI receiving sensor. In this paper, a differential MI sensor based on two ferromagnetic cores is proposed as a receiving sensor, unlike the air coil-type MI sensor in the conventional search coil sensor concept. This differential MI sensor has the advantages of ultra-high sensitivity characteristics of the pT/$\sqrt{}$Hz level, which can detect weak magnetic fields in magnetic communication; moreover, the sensor is smaller than a conventional air coil MI sensor. The proposed differential MI sensor contributes to improving sensor performance by increasing its signal-to-noise ratio. The design and fabrication of the proposed MI sensor were based on a printed circuit board (PCB). The pickup coil of the PCB-based MI sensor directly wound the pickup coil onto a ferromagnetic core composed of Ni-Zn ferrite material. To analyze the key factors that affected the performance of the receiver, the magnetic field-to-voltage conversion ratio (MVCR) and equivalent magnetic spectral density measurements of the proposed PCB-based MI sensor were performed. Wireless digital communication using quadrature phase shift keying (QPSK), which is less sensitive to noise and has a high data rate, was used to evaluate the proposed MI-based receiver. The transmitted and received waveforms were compared to confirm that the transmitted digital data were accurately received as a result of the final demodulation of the receiver. Additionally, several performance metrics, such as constellation and error vector magnitude, were measured. The results of the comprehensive analysis confirmed the applicability of the proposed differential MI-based receiver to a magnetic field.

INDEX TERMS Magnetic induction sensor, magnetic induction-based receiver, ferromagnetic core, magnetic communication.

I. INTRODUCTION

Wireless communication systems are based on radio frequency (RF) bands, which typically vary from 1 MHz to 6 GHz [1], [2]. For example, Wi-Fi operates at 2.45 GHz, most cellular networks operate from 800 MHz to 3 GHz, and millimeter waves use 28–60 GHz [3]. However, in many applications, RF communications may not be able to provide good signal quality. For example, in underwater sensor networks, RF signals can quickly fade after depths of 1 m. In underground mine exploration systems, communication devices usually cannot reach each other through RF channels if they are more than 10 m apart. In these applications, non-RF wireless media, such as magnetic or acoustic channels, may play more important roles because of their strong penetration capability in water/ground environments [1]. Specifically, magnetic induction (MI) is a reliable and high-speed wireless communication method in underwater environments.

The associate editor coordinating the review of this manuscript and approving it for publication was Wuliang Yin.

While acoustic signals propagate at an extremely slow speed (∼1,500 m/s), MI waves propagate at a speed of 3.33×10^7 m/s. When the acoustic data rate is ∼kb/s, MI can reach ∼Mb/s. In inland water (e.g., fresh water), MI can easily reach >50 m transmission distance without significant fading loss. Moreover, compared with acoustical communication, the advantages of MI communication include a scalable bandwidth over a wider spectral range, negligible propagation delay, and less susceptibility to surroundings [2]. This MI communication technique is insensitive to water turbidity, water depth, reflections by materials and surfaces, interference by sound and light, and Doppler spread and delay spread. In addition, using a magnetic field with the MI communication technique could solve the wireless communication problem of multipath propagation and fading with respect to conventional communication techniques using electromagnetic (EM) waves [4], [5], [6]. Because of these advantages, our research team implemented an MI-based receiver using a MI sensor at pT/$\sqrt{}$Hz levels that detected weak magnetic field signals as a receiving element, and aims to achieve magnetic communication over tens to hundreds of meters in underwater and underground media conditions. An important aspect of magnetic communication is an increased magnetic field-to-voltage conversion ratio (MVCR), which is expressed in V/T units, to detect weak magnetic fields [7]. Several magnetometers, known as magnetic sensors, are available, such as fluxgate, giant magneto-impedance (GMI), anisotropic magneto-resistive (AMR), giant magneto-resistive (GMR), and tunneling magnetoresistance (TMR) [7], [8], [9], [10], [11], [12], [13], [14], [15], [16], [17]. These magnetic sensors are known to have high sensitivity characteristics [8]. Specifically, the MI sensor based on a ferromagnetic core [18], [19], [20] has a sensitivity within tens of pT/$\sqrt{}$Hz, which is superior to the above-mentioned sensitivity of magnetic sensors. This MI sensor also has the advantages of small size, low cost, and easy implementation, so it could be a viable alternative for use as a receiving element in magnetic communication.

A review of the literature revealed several previous MI-based communication systems for underground and underwater applications [21], [22], [23], [24], [25], [26], [27], [28], such as two low-frequency MI-link systems, MI communications, and MI localization [22], [26], [27], [28].

However, the topic of this paper is not the MI communication link and the MI communication system. In this research, we focused on experimental verification by designing and manufacturing an MI-based receiver with a very low-frequency band for application in magnetic communications in underground and underwater environments. As described above, as the receiving element of the MI-based receiver, an MI sensor based on a ferromagnetic core with ultra-high sensitivity characteristics was used instead of the commonly used air coil-type MI sensor or receiving loop antenna. The advantage of the MI sensor is that it can have ultra-high sensitivity characteristics due to its ferromagnetic core with high permeability, which can increase the communication range of the receiver. In addition, an MI sensor based on a ferromagnetic core has advantages in size, mass, and performance compared to an air coil-type MI sensor or receiving loop antenna [1], [18], [19]. Therefore, the volume of the MI sensor-based receiver can be drastically reduced compared with the volume of the loop antenna-based receiver.

Previous studies have been conducted on magnetic sensor-based receivers to increase the range of magnetic communication [29], [30], [31], [32]. Specifically, as a detector, the AMR sensor was applied to an MI communication system [29]. This AMR detector was presented as a small, lightweight receiver unit suitable for mobile applications. However, the sensitivity of the AMR detector was nT/$\sqrt{}$Hz, which is lower than that of the MI sensor based on the ferromagnetic core of pT/$\sqrt{}$Hz. In [29], the design of the AMR-based receiver and experimental verification were not presented in detail. A GMI-based receiver for magnetic communication was presented in [30]. The results of on-off keying (OOK) demodulation at 60 kHz using the GMI-based receiver were presented. Compared with the proposed MI-based receiver, in the case of the GMI-based receiver, there was a limitation in having the complicated configuration of the receiver. The reason is that, an additional configuration was required to apply the excitation frequency and DC bias to the GMI sensor, which determined its sensitivity and magnetic noise level. In addition, because the GMI-based receiver had a super-heterodyne topology, a local frequency had to be applied, which could have increased the complexity of the receiver. OOK modulation is the simplest modulation method, but it has the limitations of vulnerability to noise and a slow data rate. Therefore, the GMI-based receiver configuration and the OOK modulation method are sensitive factors in increasing the communication range in magnetic communication.

To solve the limitations of the GMI-based receiver and increase its magnetic communication range, this paper proposes an MI-based receiver that uses a ferromagnetic core-based MI sensor as a receiving element. An MI sensor that does not require an excitation frequency or DC bias could reduce the complexity of an MI-based receiver. The sensitivity of the MI-based receiver proposed in this paper, which corresponds to the equivalent magnetic noise spectral density (EMNSD), exhibited ultra-high sensitivity within 2 pT/$\sqrt{}$Hz. The MVCR of the proposed MI sensor also exhibited approximately 268 kV_{rms}/T. Accordingly, it can increase the range of communication. In this paper, a differential MI sensor [33], [34] with two ferromagnetic cores is proposed as a receiving element instead of a conventional MI sensor based on a ferromagnetic core [18], [19], [20]. Generally, the differential MI sensor reduces common mode noise, and the output voltage of the sensor shows increased characteristics compared with the conventional MI sensor. In other words, the signal-to-noise ratio of the sensor tends to increase, which can contribute to improving the performance of the sensor. Therefore, an MI-based receiver of differential type in which a differential MI sensor is considered a receiving element

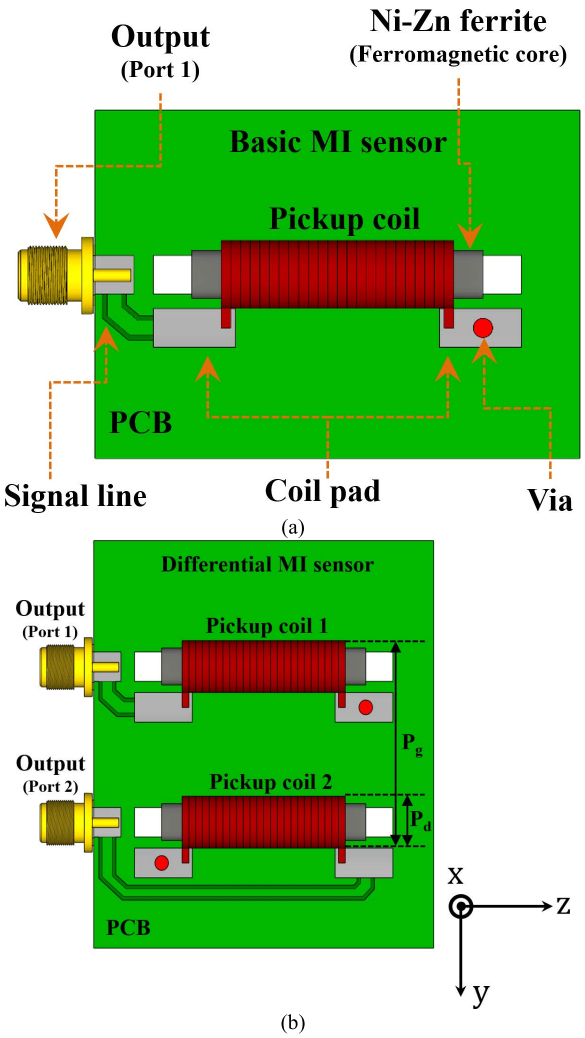

FIGURE 1. Schematic view of the proposed magnetic induction (MI) sensors: (a) basic MI sensor. (b) differential MI sensor.

is proposed. To determine its application to magnetic communication, an experimental evaluation was performed on the proposed MI sensor and differential MI-based receiver at the laboratory level by replacing the transmission antenna by a Helmholtz coil. In the proposed MI-based receiver, the quadrature phase shift keying (QPSK) modulation method, which is less sensitive to noise and has a high data rate, was adopted, and an experimental evaluation was performed.

The remainder of this paper is structured as follows: Section II presents the design of an MI sensor. A receiving element that replaces a receiving loop antenna or air coil-type MI sensors for magnetic communication is designed as a magnetic sensor based on a ferromagnetic core. Section III describes the system configuration for the experimental evaluation of the proposed MI sensor and the MI-based receiver. Section IV describes the measurement strategies and discusses the results of the experimental evaluation of the proposed MI sensor and the MI-based receiver. Concluding remarks and recommendations for future work are provided in section V.

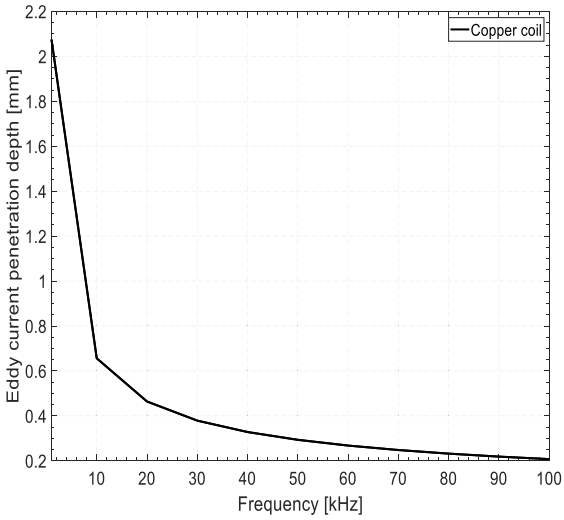

FIGURE 2. Eddy current penetration depth of the copper coil for the MI sensor as a function of frequency.

TABLE 1. Design parameters of MI sensors.

Parameter	Basic MI sensor	Differential MI sensor
Core diameter	5 mm	5 mm
Core length	30 mm	30 mm
Number of cores	1	2
Number of turns of the pickup coil	3000	3000
Width of the pickup coil	25 mm	25 mm
Outer diameter of the pickup coil (P_d)	7.5 mm	7.5 mm
Gap between two pickup coils (Pg)	-	28.5 mm
Overall PCB Size	45 × 35 × 1.6 mm^3	50 × 55 × 1.6 mm^3

II. DESIGN PROCEDURE

A. DESIGN OF AN MI SENSOR

Fig. 1 shows the structure of the proposed MI sensor designs for use as a receiving element to replace a receiving loop antenna or air coil-type MI sensors in magnetic communication. The considered magnetic material used in the ferromagnetic core was Ni-Zn soft ferrite with a relative permeability of 700. The shape of the ferromagnetic core is cylindrical, and the size has a diameter of 5 mm and a length of 30 mm. The MI sensors are based on a printed circuit board (PCB) substrate with FR4 material composed of a relative permittivity of 4.6.

As shown in Fig. 1(a), a basic MI sensor was designed to compare and verify the performance of the differential MI sensor shown in Fig. 1(b), which was used as the receiving sensor in the differential MI-based receiver.

As shown in Fig. 1(a), the PCB-based MI sensor directly wound the pickup coil onto the cylindrical ferromagnetic

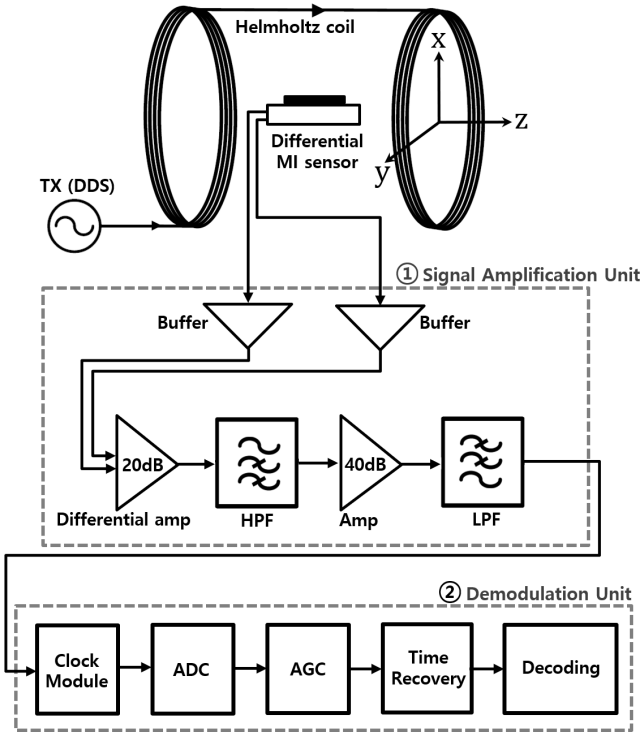

FIGURE 3. Block diagram of the differential MI-based receiver.

core. An enameled copper wire 0.1 mm in diameter was used for the pickup coil, the width of which was 25 mm. Here, the wire diameter of the copper wire was selected in consideration of the eddy current penetration depth of the copper wire. This is because both the inductance and the quality factor of the coils at radio frequencies with respect to the eddy current penetration depth are affected by the eddy current flow in the highly conductive ferromagnetic core. In particular, with increasing frequency, the eddy current loss increases rapidly as the skin depth of the ferromagnetic core became smaller than the core thickness. Therefore, the eddy current penetration depth of the copper wire corresponding to the pickup coil was analyzed according to the frequency. The eddy current penetration depth was defined by equation $\delta = \sqrt{\frac{2\rho}{\mu\omega}}$. where ρ is the resistivity of the copper and its value is $1.7 \times 10^{-8}\Omega m$, μ is the permeability of copper(i.e., corresponding to $\mu_r \times \mu_0$, $\mu_r = 1$, $\mu_0 = 4\pi \times 10^{-7} H/m$), and ω is the angular frequency. Fig. 2 shows the calculated eddy current penetration depth for the copper coil of the MI sensor as a function of frequency using the equation of eddy current penetration depth. The frequency considered for magnetic communication in this paper is 20 kHz. The calculated eddy current penetration depth of the copper coil was approximately 0.46 mm at 20 kHz. The wire diameter of the copper pickup coil of the MI sensor considered was 0.1 mm, and the wire diameter of the copper coil within the eddy current penetration depth was selected. The total number of turns on the pickup coil was 3,000 in 12 layers, at 250 turns per layer. The pickup coil was soldered to the coil pad. The left side of the coil pad was connected to port 1 along a signal line. The right side of the coil pad was connected to the ground through a via.

Fig. 1(b) shows the differential type of PCB-based MI sensor. In the proposed differential MI sensor, a pickup coil configuration was added to the basic MI sensor structure shown in Fig. 1(a). This differential MI sensor has a differential connection between the pickup coil and the port: the starting point of pickup coil 1 is connected to port 1, and the end point of pickup coil 2 is connected to port 2. Accordingly, the pickup coil in the proposed differential MI sensor measures the same field but in the opposite direction. For this reason, the current directions of the two pickup coils (pickup coil 1 and pickup coil 2) are opposite to each other, and a 180° phase difference occurs between the two coils. In addition, this differential MI sensor could produce twice the magnitude of the induced voltage with a 180° phase difference, which contributed to improving its performance. The design parameters of the proposed MI sensors are presented in Table 1.

B. DESIGN OF AN MI-BASED RECEIVER

Fig. 3 shows a block diagram of the detailed structure of the differential MI-based receiver. The signal was digitally modulated in the direct digital synthesis (DDS) of the transmitter (Tx) and sent to the Helmholtz coil. The Helmholtz coil acts as a transmitting antenna and transmits a modulated signal to the receiver (Rx).

The differential MI sensor, which is the receiving element of the Rx, detects a modulated signal. Here, the differential MI sensor was placed in the zy-plane inside the center of the Helmholtz coil, and two ferromagnetic cores wound around the pickup coils in the differential MI sensor were located along the z-axis to detect the modulated signal. In addition, the magnetic field (i.e., corresponding to the magnetic flux density) of the Helmholtz coil in Fig. 3 (i.e., corresponding to the fabricated Helmholtz coil in Fig. 4) used as a signal source was measured. Fig. 5 shows the magnetic field measurement results in the z-axis of the Helmholtz coil. The measured average uniform magnetic field was $106.7 \pm 0.5\mu$T, and the range of the uniform magnetic field was 70 mm. The size of the differential MI sensor is smaller than the range of measured uniform magnetic field. Moreover, in the differential MI sensor, the gap between the two pickup coils (pickup coil 1 and pickup coil 2, P_g in Table 1) was 28.5 mm, which is smaller than the measured uniform magnetic field range of 70 mm. Accordingly, a uniform magnetic field is generated along the z-axis of the Helmholtz coil, and the differential MI sensor detects a magnetic field signal within a uniform magnetic field. The differential MI-based receiver consisted of two parts. The first part of the MI-based receiver was the signal amplification unit (i.e., corresponding to ① of the differential MI-based receiver shown in Fig. 4(b)). This part consists of analog RF circuits. The second part of the MI-based receiver is the demodulation unit (i.e., corresponding to ② of the differential MI-based receiver shown in Fig. 4(b)). This part consisted of an oscilloscope onboard module mounted on

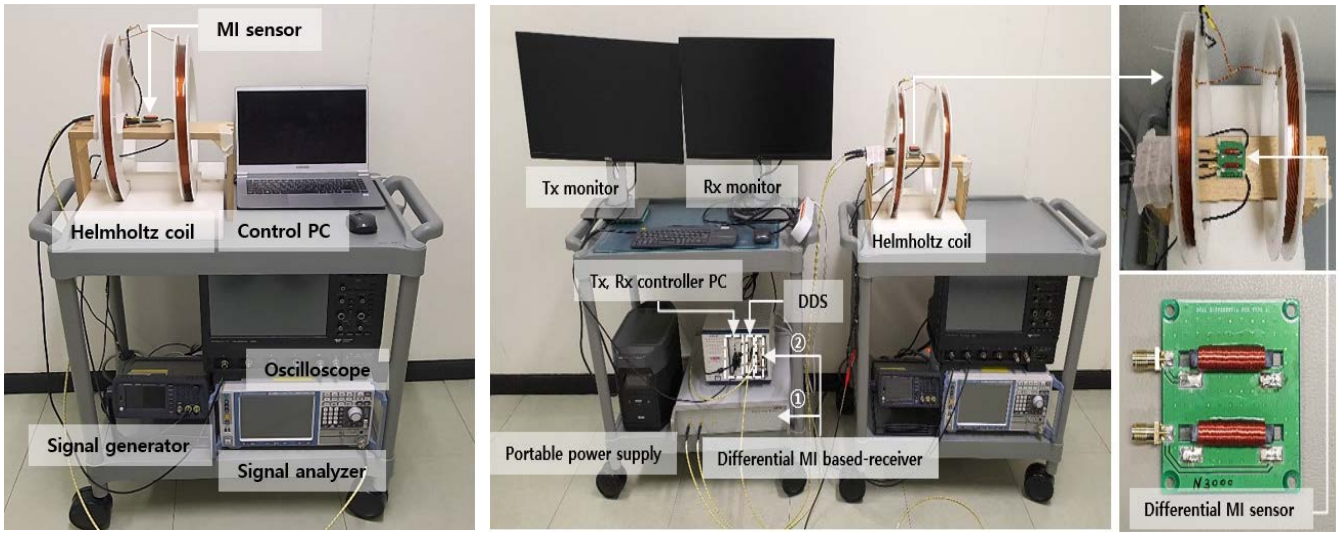

(a) (b)

FIGURE 4. Experimental environment configuration : (a) MI measurement system; (b) MI based-receiver evaluation system.

a Tx, Rx controller PC (omitted from Fig. 3; see Fig. 4). Therefore, it could be implemented as digital demodulation processing in the Tx, Rx controller PC.

III. SYSTEM CONFIGURATION

The experimental measurement environment of the designed MI sensor and MI-based receiver for the experimental evaluation of the magnetic communication possibility was configured (see Fig. 4).

A. EXPERIMENTAL SETUP AND CONFIGURATION OF AN MI SENSOR

Fig. 4(a) shows the configuration of the experimental environment (i.e., an MI measurement system) of the proposed MI sensor. The key characteristics of the proposed MI sensor were assessed using the MI measurement system.

The Helmholtz coil was used as a transmitting antenna. It transmitted an external AC magnetic field to the MI sensor when the external AC magnetic field was generated in the signal generator (Keysight, 33500B) and fed to the Helmholtz coil. The magnetic flux density generated inside the Helmholtz coil, where the MI sensor was located, was defined by the equation $B = (4/5)^{3/2}\mu_0 NI/R$, where μ_0 is the permeability constant, I is the current applied to the Helmholtz coil, and N and R are the turns and radius of the Helmholtz coil, respectively [35].

A signal analyzer (Rohde & Schwarz, FSV4), oscilloscope (Teledyne LeCroy, Wavesurfer 510), and LCR meter (HIOKI, IM3536, omitted from Fig. 4) were used to collect the output data from the MI sensor. The MI measurement system was operated through a control PC.

B. EVALUATION SYSTEM CONFIGURATION FOR AN MI-BASED RECEIVER

Fig. 4(b) shows the experimental evaluation system of the differential MI-based receiver. To verify the possibility of magnetic communication, the modulation signal with a message signal was in the QPSK modulation format.

The modulation signal with message data was generated by the DDS (National Instruments, PXIe-5442) mounted in the Tx, Rx controller PC, converted into an analog signal, and sent to the Helmholtz coil. The Helmholtz coil with $N = 90$ turns and $R = 150$ mm transmitted an analog modulation signal to the differential MI sensor. The differential MI sensor detected an analog modulation signal and sent it to the signal amplification unit (i.e., corresponding to ① of the differential MI-based receiver shown in Fig. 4(b)) of the differential MI-based receiver. In this stage, the signal amplifier unit was responsible for amplifying the analog modulation signal and removing harmonic bands outside the passband. The Tx, Rx controller PC with the demodulation unit (National Instruments, PXIe-5122) of the proposed MI-based receiver (i.e., corresponding to ② of the differential MI-based receiver shown in Fig. 4(b)) decoded the modulation signal received from the signal amplification unit and output it to the Rx monitor.

IV. RESULTS AND DISCUSSION

This section discusses the results of the experimental evaluation of the proposed MI sensor and the MI-based receiver. To verify magnetic communication, we chose the lowest frequency band (19 kHz–21 kHz) recommended by the International Telecommunication Union-Radio communication Sector/Study Groups 1 (ITU-R/SG1) as standards of wireless power transmission. Therefore, the experimental results were based on a center frequency of 20 kHz, corresponding to an external AC magnetic field.

A. EVALUATION OF A MI SENSOR

The experimental evaluation was conducted on the proposed MI sensors using the experimental measurement environment shown in Fig. 4(a).

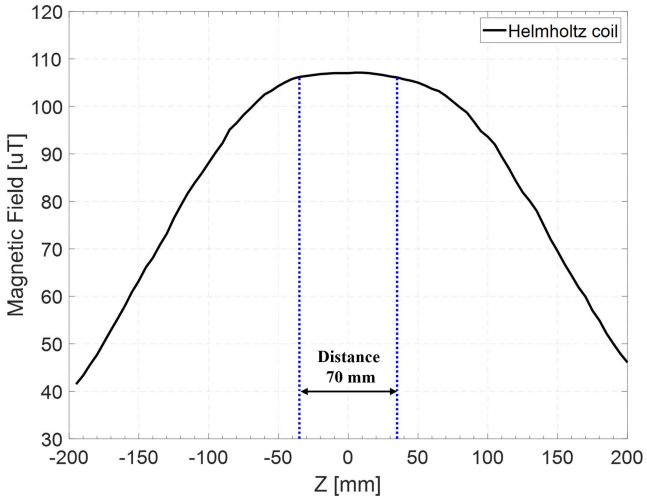

FIGURE 5. Magnetic field measurement results in the z-axis of the Helmholtz coil.

The characteristics of the sensing elements that determine the performance of a sensor, such as induced voltage, MVCR, voltage noise spectral density, and equivalent magnetic spectral density, were assessed using an MI measurement system.

A voltage applied to the Helmholtz coil uses a voltage change from 0.001 Vpp to 10 Vpp, which represented a change in its magnetic field strength. At this time, the magnetic field strength was as high as 1μT, as shown in Fig. 6. The induced voltage with a unit of mVrms, which represented the dynamic range of MI sensors, and the MVCR with a unit of kV/T, are shown in Fig. 6. The general induced voltage of the MI sensor with the ferromagnetic core was defined as follows [18], [19], [20]:

$$v_{out} = -\frac{d\phi}{dt} = -\frac{NA\mu_0\mu_r dH}{dt} = -\frac{NAdB}{dt} \tag{1}$$

When the sinusoidal magnetic flux density $B = B_0 \sin \omega t = \mu_0\mu_r H_0 \sin(\omega t)$ was considered, the induced voltage of the pickup coil for the MI sensor was written as follows:

$$v_{out} = -NA\omega\mu_0\mu_r H_0 \cos(\omega t) \tag{2}$$

where Φ is the time varying magnetic flux passing through a pickup coil of the MI sensor, N is the turns of the pickup coil, A is the cross-section area of the ferromagnetic core, μ_0 is the permeability constant, and μ_r is the relative permeability of the ferromagnetic core. Improving the values of these parameters increases the induced voltage and sensitivity of the sensor. However, the improving effect of these parameters is limited because raising these parameters may amplify thermal and magnetic noises [20]. Therefore, it is necessary to design a sensor that considers the optimization of these parameters, and the induced voltage of the MI sensor was measured taking this into consideration. The measured induced voltage shown in Fig. 6(a) is the induced voltage obtained as the root mean square (RMS) of the v_{out} in Eq. (2). From Eq. (2), the MVCR of the MI sensor shown in Fig. 6(b)

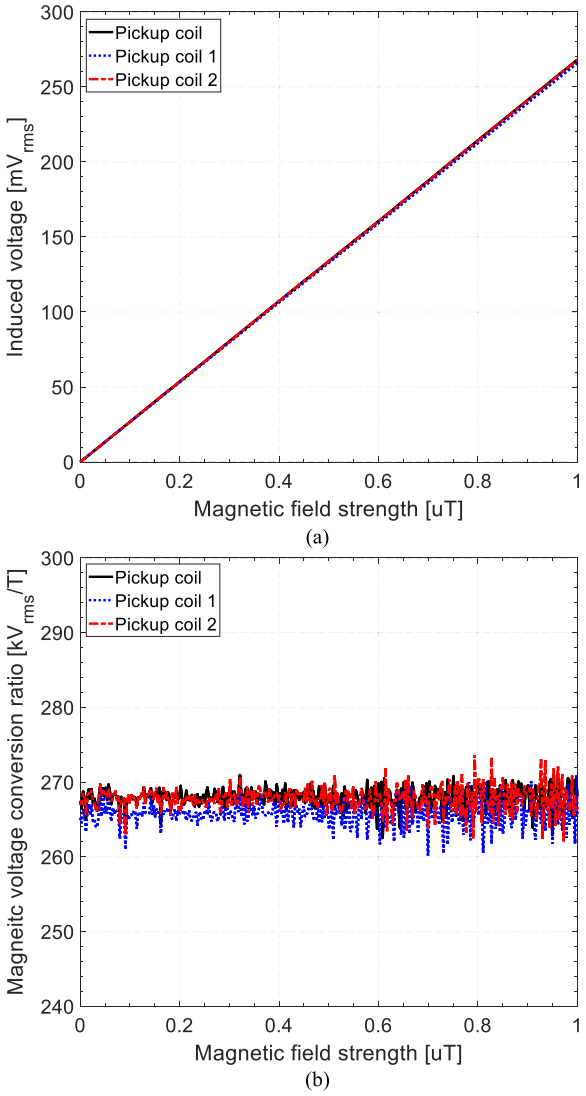

FIGURE 6. Results of the induced voltage and magnetic voltage conversion ratio (MVCR) of the basic MI sensor and differential MI sensor: (a) Induced voltage at 20 kHz; (b) MVCR at 20 kHz.

was obtained by the slope of the induced voltage shown in Fig. 6(a).

Fig. 6 shows the measured induced voltage and MVCR of the two proposed MI sensors at an external frequency of 20 kHz. When the Helmholtz coil was operated at 20 kHz, the resistance of the Helmholtz coil was 1.68 kΩ. An induced voltage of up to 267.8 mV_{rms} and an MVCR of 268 kV_{rms}/T were achieved using the basic MI sensor with the pickup coil. The achieved induced voltage and MVCR were 266.6 mV_{rms} and 267 kV_{rms}/T in pickup coil 1 in the differential MI sensor and 267.6 mV_{rms} and 268 kV_{rms}/T in pickup coil 2 in the differential MI sensor, respectively. These results confirmed the highly linear characteristics of the induced voltage under a magnetic field of up to 1×10^{-6} tesla. Here, in order to evaluate the measured MVCR of the differential MI sensor, an initial evaluation of the theoretical limit of MVCR for the differential MI sensor is required. An initial evaluation of the

TABLE 2. Performance metrics of the proposed MI sensors.

Frequency [kHz]	Dynamic range [mV_{rms}]			MVCR [kV_{rms}/T]			Average VNSD [$nV_{rms}/\sqrt{Hz}$]			Average EMNSD [$pT/\sqrt{Hz}$]		
	Basic MI Pickup coil	Differential MI Pickup coil 1	Differential MI Pickup coil 2	Basic MI Pickup coil	Differential MI Pickup coil 1	Differential MI Pickup coil 2	Basic MI Pickup coil	Differential MI Pickup coil 1	Differential MI Pickup coil 2	Basic MI Pickup coil	Differential MI Pickup coil 1	Differential MI Pickup coil 2
20	Max. 267.8	Max. 266.6	Max. 267.6	268	267	268	450	350	500	1.68	1.31	1.86

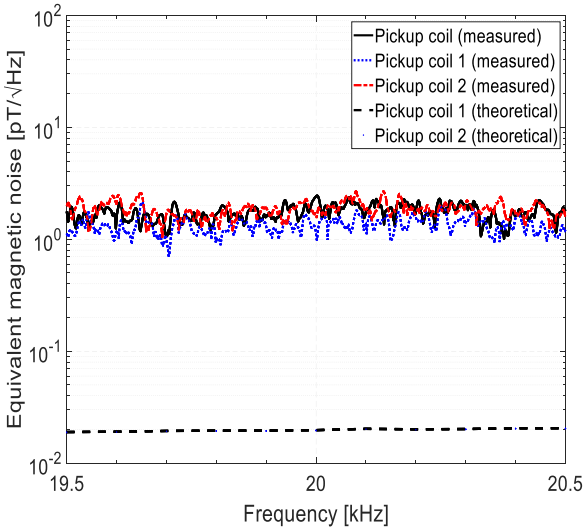

FIGURE 7. Equivalent magnetic noise spectral density (EMNSD) of the MI sensors to which MVCR of each MI sensor is applied.

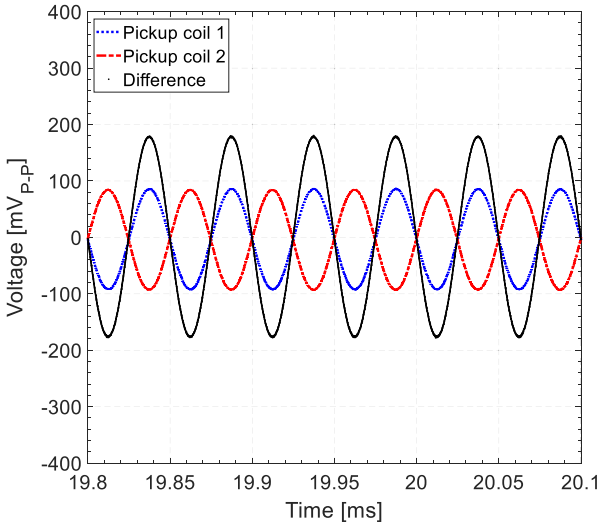

FIGURE 8. Output voltage characteristics at 20 kHz for each pickup coil of a differential MI sensor in the time domain.

theoretical limit of the MVCR for the proposed differential MI sensor was performed using Eq. (19) in the literature [19]. The equation is defined as follows:

$$S = \frac{S_0}{\sqrt{(1+\alpha)^2 + (\beta^2 + \frac{\partial^2}{\beta^2} - 2)\cdot\gamma^2 + \gamma^4}} \tag{3}$$

where α is a coefficient that can be expressed as $\alpha = R/R_0$, R is the resistance of the pickup coil, and R_0 is the load resistance (i.e., corresponding to the input resistance of the voltage buffer connected to the output of the pickup coil, $R_0 = 2 \times 10^4\Omega$). The factor $\beta = R\sqrt{C/L}$ is considered, the factor $\gamma = 2\pi f\sqrt{LC}$ is written, f is the center frequency, L is the inductance of the pickup coil, and C is the parasitic capacitance of the pickup coil. The absolute sensitivity S_0 can be described as $S_0 = 2 \times 10^{-7}\pi^3 N D^2$, where N is the number of turns of the pickup coil ($N = 3000$), and D is the outer diameter of the pickup coil (see Table 1, P_d =7.5 mm). The MVCR of the differential MI sensor was calculated using Eq. (3). The values obtained from the impedance measurement results in Fig. 10(a) were used for the R, L, and C values of the pickup coil used in the calculation.

The calculated MVCR of pickup coil 1 in the differential MI sensor is 294 kV_{rms}/T at 20 kHz, and the calculated MVCR of pickup coil 2 in the differential MI sensor is 296 kV_{rms}/T at 20 kHz. Therefore, the measured MVCR of the differential MI sensor is lower than that of the calculated differential MI sensor. Consequently, it was confirmed that the measured MVCR of the differential MI sensor was well measured below the theoretical limit.

In addition, the induced voltage and MVCR results showed performance characteristics similar to both the basic MI sensor and the differential MI sensor. In addition, similar to the results of the induced voltage characteristics and MVCR characteristics, the performance characteristics of each pickup coil wound on the ferromagnetic core of the differential MI sensor were almost the same within the measurement error range.

Fig. 7 shows the EMNSD of the proposed MI sensors obtained from the signal analyzer. The frequency bandwidth for the EMNSD measurements was 19.5–20.5 kHz. The EMNSD e_n in magnetic communication determines the weakest detectable magnetic signals, which can be obtained by dividing the voltage noise spectral density (VNSD) v_n with units of $nV_{rms}/\sqrt{Hz}$ into the MVCR S_v. It was defined as follows:

$$e_n = \frac{v_n}{S_v} \tag{4}$$

The units of the EMNSD are $T/\sqrt{Hz}$.

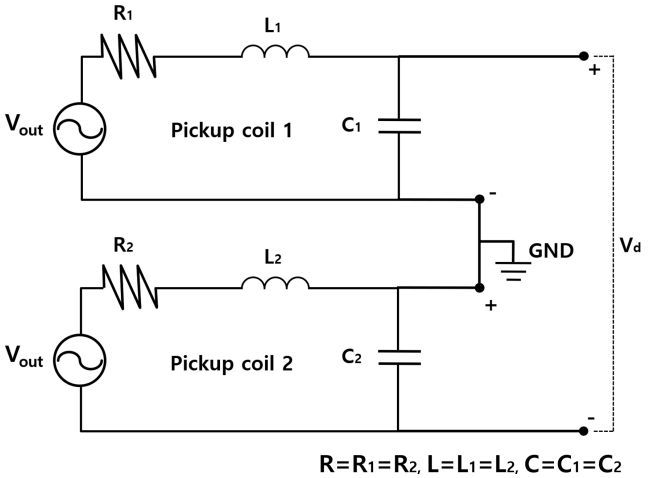

FIGURE 9. Electrical circuit model of the differential MI sensor.

Regarding the basic MI sensor with the pickup coil, at a center frequency of 20 kHz, with an MVCR of 268 kVrms/T and an average VNSD of 450 nVrms/$\sqrt{}$Hz, the average EMNSD was 1.68 pT/$\sqrt{}$Hz. The results of MVCR and average VNSD shown in Table 2 were applied; the average EMNSD was 1.31 pT/$\sqrt{}$Hz at 20 kHz for pickup coil 1 in the differential MI sensor and 1.86 pT/$\sqrt{}$Hz at 20 kHz for pickup coil 2 in the differential MI sensor. In order to evaluate the measured EMNSD of the differential MI sensor, an initial evaluation of the theoretical limit of noise for the differential MI sensor was performed. A thermal noise equation, one of the intrinsic noises of the sensor, was used to theoretically calculate and evaluate the sensor noise. Because the proposed differential MI sensor has a structure with a pickup coil, thermal noise depends on the electrical resistance of the coil. Therefore, an increasing number of turns, can increase the thermal noise because it raises the resistivity. As a result, the evaluation of the theoretical limit on the noise of the sensor can be replaced with the thermal noise (or Johns noise) on the pickup coil of the differential MI sensor. The thermal noise was defined by equation $e_t = 2\sqrt{k_B T R \Delta f}$. where k_B is the Boltzmann's constant, R is the resistance of the pickup coil, T is the room temperature in Kelvin (T = 300 K), and Δf is the bandwidth in hertz. The calculated thermal noise for pickup coil 1 in the differential MI sensor was 5.80 $nV_{rms}/\sqrt{}$Hz at 20 kHz, and the calculated thermal noise for the pickup coil 2 in the differential MI sensor was 5.59 $nV_{rms}/\sqrt{}$Hz at 20 kHz, respectively. The measured VNSD of the differential MI sensor was measured below the calculated thermal noise. The EMNSD for the differential MI sensor was calculated by considering the theoretically calculated MVCR and the thermal noise. The calculated EMNSD for pickup coil 1 in the differential MI sensor was 19.7 fT/$\sqrt{}$Hz at 20 kHz, and the calculated EMNSD for pickup coil 2 in the differential MI sensor was 18.9 fT/$\sqrt{}$Hz at 20 kHz. The calculated EMNSD results are shown in Fig. 7. As a result, the measured EMNSD of the differential MI sensor was below the calculated EMNSD of the differential MI sensor, and acceptable results were obtained.

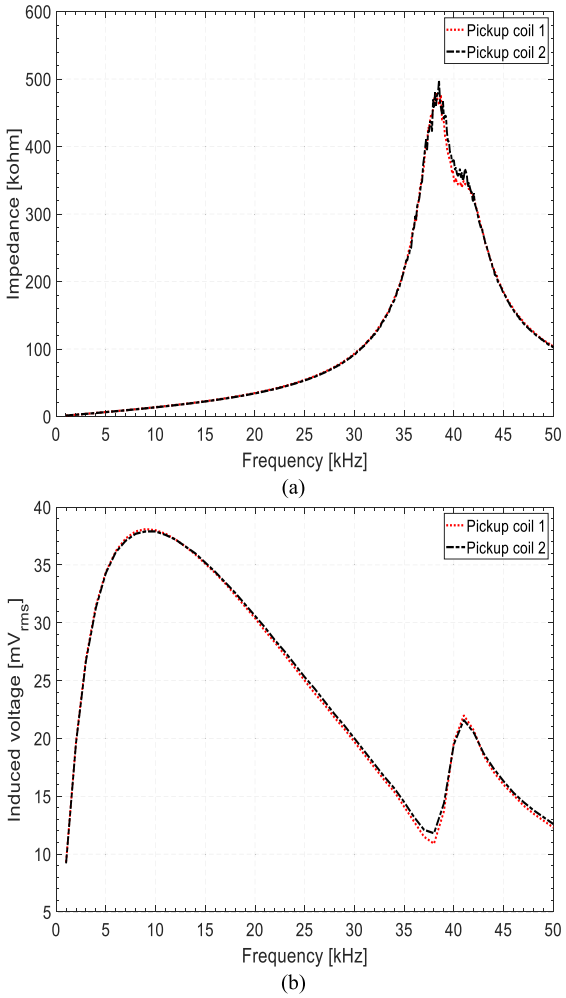

FIGURE 10. Frequency dependence for each pickup coil of the differential MI sensor: (a) Measured impedance; (b) Measured induced voltage.

In addition, in the two types of MI sensors, the overall EMNSD characteristics of the considered frequency bandwidth showed almost similar noise characteristics in the range of 1–2 pT/$\sqrt{}$Hz. It was confirmed that the MI sensors showed excellent equivalent magnetic noise characteristics at the pT/$\sqrt{}$Hz levels. The results of the experimental evaluation of the proposed MI sensors are summarized in Table 2.

In addition, to check the output voltage characteristics of the two pickup coils in the differential MI sensor, measurements were performed in the time domain, the results of which are shown in Fig. 8. Here, using Eq. (1), the output voltage characteristic of the differential MI sensor can be written as follows [32]:

$$v_d = v_{pickup2} - v_{pickup1} = \frac{NAdB}{dt} - \left(-\frac{NAdB}{dt}\right) = \frac{2NAdB}{dt} \tag{5}$$

where v_d is the difference voltage corresponding to the difference in the output voltage of each pickup coil in the differential MI sensor. In general, the MI sensor can be represented by an electrical circuit model [36]. Thus, the differential

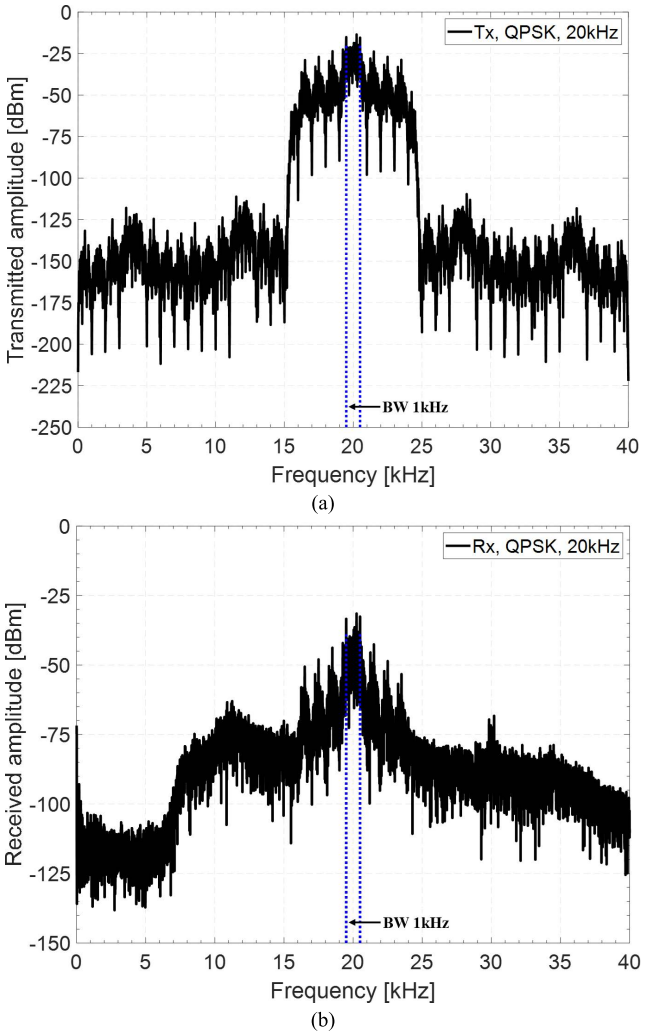

FIGURE 11. Analog waveform of signals modulated and demodulated with QPSK at carrier frequency of 20 kHz in the frequency domain: (a) Transmitted analogue waveform with a BW of 1 kHz; (b) Received analogue waveform with a BW of 1 kHz.

MI sensor can also be represented by an equivalent circuit corresponding to the electrical modeling as shown in Fig. 9. For this electrical model, using Eq. (2) corresponding to the induced voltage of the basic MI sensor, the difference voltage to the frequency response characteristic can be written as follows:

$$\begin{aligned} v_d &= v_{pickup2} - v_{pickup1} \\ &= \frac{NA\omega B}{\left(1-\omega^2 LC\right)+j\omega RC} - \left(-\frac{NA\omega B}{\left(1-\omega^2 LC\right)+j\omega RC}\right) \\ &= \frac{2NA\omega B}{\left(1-\omega^2 LC\right)+j\omega RC} \end{aligned} \tag{6}$$

where, the R_1 and R_2 are each coil resistance in the differential MI sensor, L_1 and L_2 are each coil inductance, C_1, and C_2 account for the parasitic capacitance by the turns of each coil for the two pickup coils. From Eq. (5) and Eq. (6), it was confirmed that the magnitude of the output voltage in the differential MI sensor was twice the magnitude of the output voltage by one pickup coil.

When the voltage applied to the Helmholtz coil was 1 V_{pp}, and the converted magnetic flux density was B = 0.114 μT, the phase difference between the two coils of the differential MI sensor was 180°. In addition, the output voltage of pickup coil 1 in the differential MI sensor measured by the oscilloscope was approximately 180 mV_{pp} at 20 kHz. In pickup coil 2, the measured output voltage was approximately 180 mV_{pp} at 20 kHz. The difference between the output voltages in the two pickup coils was approximately 360 mV_{pp}. This result agrees with the theoretical results of Eq. (5) and Eq. (6). Therefore, it was confirmed that the differential MI sensor could improve sensor performance because the output voltage was twice the output voltage of one pickup coil. Based on the results, the differential MI sensor was well designed, which confirmed its suitability for use as a receiving element in the proposed MI-based receiver instead of the basic MI sensor.

To investigate the performance characteristics of the proposed differential MI sensor in different frequency bands, the impedance and induced voltage characteristics were analyzed.

The measured impedance characteristics of the two pickup coils of the differential MI sensor using the LCR meter exhibited almost the same characteristics in the 1 kHz–50 kHz frequency bands as shown in Fig. 10(a). It can be seen that LC resonance occurs owing to the inductance (L) of the pickup coil and the parasitic capacitance (C) caused by the turns of the pickup coil near the 40 kHz band. From these results, the magnetic field-to-voltage conversion ratio (MVCR), which corresponds to the sensitivity of the sensor, can be maximized near the 40 kHz frequency band.

However, as observed from the results in Fig. 10(b), the induced voltage characteristics of the two pickup coils constituting the differential MI sensor were superior in the 20 kHz frequency band than in the 40 kHz band. In addition, to use the differential MI sensor as a receiving element for magnetic communication, the bandwidth of the differential MI sensor, which is a receiving element, should be wide and stable output voltage characteristics are required. Therefore, it is advantageous in terms of the bandwidth of magnetic communication to use 20 kHz rather than 40 kHz, where resonance occurs.

B. EVALUATION OF AN MI-BASED RECEIVER

The experimental assessment of the MI-based receiver was performed using the MI-based receiver evaluation system shown in Fig. 4(b). The experimental results are shown in Fig. 10 and Fig. 11. The carrier frequency of the QPSK modulation was 20 kHz, which corresponded to the external AC frequency. The symbol rate and data rate used in the QPSK modulation and demodulation experiments were 1 kHz and 2 kbps, respectively.

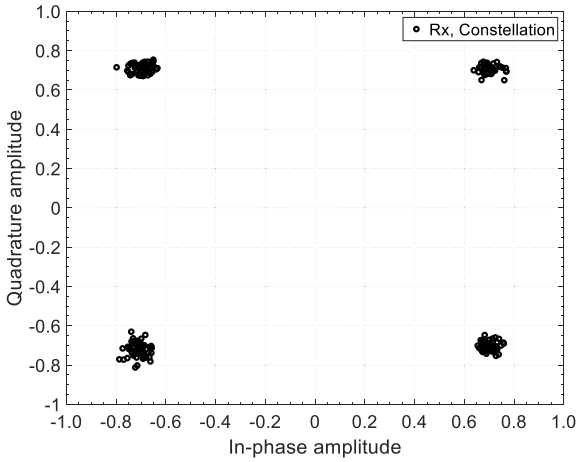

FIGURE 12. QPSK constellation result.

Fig. 11(a) shows the analog waveform transmitted when 1 V_{pp} was applied by the DDS of Tx in the frequency domain. The converted external magnetic flux density at the location of the differential MI sensor from the Helmholtz coil was B = 0.114 μT. The bandwidth (BW) of Tx was 1 kHz. In the transmitted analog waveform shown in Fig. 10(a), the message data information of "Hello world" was included in the QPSK modulation signal.

Fig. 11(b) shows the results of the QPSK demodulation of Rx in the frequency domain. The received analog waveform of Rx confirmed that the modulation signal, including the message data and the BW of 1 kHz sent from Tx, was received effectively.

Fig. 12 shows the constellation results for the demodulation of the QPSK. The demodulation signal, represented by the symbol, was located at four points in the in-phase (I) and the quadrature phase (Q) plane in the complex plane. The measured symbols of amplitude and phase at each location exhibited a phase difference of 90°, respectively. The measured E_b/N_0 was 30.6 dB. Because this E_b/N_0 value was large, the symbols at each point in the four locations were well concentrated. Here, E_b is the signal energy associated with the data bit and N_0 is the noise power spectral density at the noise power of 1 Hz bandwidth. E_b/N_0 is a normalized signal-to-noise ratio (SNR) measurement value known as SNR per bit. E_b/N_0 was written as follows:

$$\frac{E_b}{N_0} = \frac{C}{N} \times \frac{R_b}{B_w} \tag{7}$$

where C is the total carrier power, N is the total noise power in the bandwidth, B_w is the channel bandwidth in Hz, and R_b is the bit rate at a unit of bits per second (bps). In addition, in the constellation shown in Fig. 12, the RMS measurement value of the error vector magnitude (EVM) was 5.6%. This result was satisfactory within 22.4%, which is the allowable range of the EVM standard of QPSK defined by IEEE 801.11ac [37], indicating characteristics. The EVM was defined as a percentage (%) as follows [38], [39]:

$$EVM(\%) = \sqrt{\frac{\frac{1}{N}\sum_{n=1}^{N}|S_n - S_{0,n}|^2}{\frac{1}{N}\sum_{n=1}^{N}|S_{0,n}|^2}} \times 100\% \tag{8}$$

where $S_{0,n}$ is the ideal normalized constellation point of the n-th symbol, S_n is the normalized n-th symbol in the stream of measured symbols, and N is the number of symbols in the constellation. These results confirmed that the proposed MI-based receiver accurately received the QPSK modulation signal with the message data by minimizing the data error. The performance results of the proposed MI-based receiver are summarized in Table 3.

TABLE 3. Performance results of the differential MI-based receiver.

Parameter	MI-based Receiver
Modulation/demodulation method	QPSK
Carrier frequency (Hz)	20 kHz
Symbol rate (Hz)	1 kHz
Data rate (bps)	2 kbps
EVM (%)	5.6
Estimated E_b/N_0 (dB)	30.6

V. CONCLUSION

This paper proposed a topology that demodulates radio signals into informative data for the use of a differential MI-based receiver in wireless communication. As a receiving element, a ferromagnetic core-based MI sensor that is a small, highly sensitive and easy to implement compared with an air coil-type MI sensor was proposed, and its key characteristics were analyzed. In addition, in order to maximize the sensitivity of the MI-based receiver, a differential MI sensor with twice the signal output and 180° phase difference compared with the basic MI sensor was analyzed. The results of the experimental verification of the implemented MI receiver showed that it accurately received and demodulated the QPSK modulation signal with the message data. In a future study, we plan to conduct communication experiments and analyses in various complex environments, such as air, underground, and underwater, using the proposed MI-based receiver by applying a practical transmission antenna as the Tx instead of the Helmholtz coil.

REFERENCES

[1] F. Hu, *Magnetic Communications: From Theory to Practice*. Boca Raton, FL, USA: CRC Press, 2018.
[2] M. Hott and P. A. Hoeher, "Underwater communication employing high-sensitive magnetic field detectors," *IEEE Access*, vol. 8, pp. 177385–177394, 2020.

[3] E. Park and S. Kim, "Design and analysis of a TEM mode rectangular coaxial waveguide for mobile 5G millimeter wave antenna module applications," *J. Electromagn. Eng. Sci.*, vol. 20, no. 3, pp. 169–175, Jul. 2020.
[4] Z. Sun and I. F. Akyildiz, "Underground wireless communication using magnetic induction," in *Proc. IEEE Int. Conf. Commun. (ICC)*, Jun. 2009, pp. 1–5.
[5] S. Wang and Y. Shin, "Efficient routing protocol based on reinforcement learning for magnetic induction underwater sensor networks," *IEEE Access*, vol. 7, pp. 82027–82037, 2019.
[6] H. Guo, Z. Sun, and C. Zhou, "Practical design and implementation of metamaterial-enhanced magnetic induction communication," *IEEE Access*, vol. 5, pp. 17213–17229, 2017.
[7] J.-Y. Kim, I.-K. Cho, H. J. Lee, J. Lee, J.-I. Moon, S.-M. Kim, S.-W. Kim, S. Ahn, and K. Kim, "A novel experimental approach to the applicability of high-sensitivity giant magneto-impedance sensors in magnetic field communication," *IEEE Access*, vol. 8, pp. 193091–193101, 2020.
[8] P. Ripka, *Magnetic Sensors and Magnetometers*. Norwood, MA, USA: Artech House, 2001.
[9] M. Malátek and L. Kraus, "Off-diagonal GMI sensor with stress-annealed amorphous ribbon," *Sens. Actuators A, Phys.*, vol. 164, nos. 1–2, pp. 41–45, Nov. 2010.
[10] F. Jin, J. Wang, L. Zhu, W. Mo, K. Dong, and J. Song, "Impact of adjustment of the static working point on the 1/f noise in a negative feedback GMI magnetic sensor," *IEEE Sensors J.*, vol. 19, no. 20, pp. 9172–9177, Oct. 2019.
[11] B. Dufay, S. Saez, C. P. Dolabdjian, A. Yelon, and D. Menard, "Characterization of an optimized off-diagonal GMI-based magnetometer," *IEEE Sensors J.*, vol. 13, no. 1, pp. 379–388, Jan. 2013.
[12] P.-H. Hsieh and S.-J. Chen, "Multilayered vectorial fluxgate magnetometer based on PCB technology and dispensing process," *Meas. Sci. Technol.*, vol. 30, no. 12, Dec. 2019, Art. no. 125101.
[13] P. Ripka, M. Janosek, and M. Butta, "Crossfield sensitivity in AMR sensors," *IEEE Trans. Magn.*, vol. 45, no. 10, pp. 4514–4517, Sep. 2009.
[14] Z. Wang, X. Wang, M. Li, Y. Gao, Z. Hu, T. Nan, X. Laing, H. Chen, J. Yang, S. Cash, and N. X. Sun, "Highly sensitive flexible magnetic sensor based on anisotropic magnetoresistance effect," *Adv. Mater.*, vol. 28, no. 42, pp. 9370–9377, 2016.
[15] F. B. Mancoff, J. H. Dunn, B. M. Clemens, and R. L. White, "A giant magnetoresistance sensor for high magnetic field measurements," *Appl. Phys. Lett.*, vol. 77, no. 12, pp. 1879–1881, 2000.
[16] J. G. Deak, Z. Zhou, and W. Shen, "Tunneling magnetoresistance sensor with pT level 1/f magnetic noise," *AIP Adv.*, vol. 7, no. 5, May 2017, Art. no. 056676.
[17] N. A. Stutzke, S. E. Russek, D. P. Pappas, and M. Tondra, "Low-frequency noise measurements on commercial magnetoresistive magnetic field sensors," *J. Appl. Phys.*, vol. 97, no. 10, p. 10Q107, 2005.
[18] A. Grosz and E. Paperno, "Analytical optimization of low-frequency search coil magnetometers," *IEEE Sensors J.*, vol. 12, no. 8, pp. 2719–2723, Aug. 2012.
[19] S. Tumanski, "Review article: Induction coil sensors—A review," *Meas. Sci. Technol.*, vol. 18, no. 3, pp. R31–R46, 2007.
[20] A. Nourmohammadi, S. M. H. Feiz, and M. H. Asteraki, "Investigation of noise reduction and SNR enhancement in search coil magnetometers at low frequencies," 2014, *arXiv:1409.7267*. [Online]. Available: https://arxiv.org/abs/1409.7267
[21] Z. Sun and I. F. Akyildiz, "Magnetic induction communications for wireless underground sensor networks," *IEEE Trans. Antennas Propag.*, vol. 58, no. 7, pp. 443–482, Apr. 2010.
[22] T. E. Abrudan, O. Kypris, N. Trigoni, and A. Markham, "Impact of rocks and minerals on underground magneto-inductive communication and localization," *IEEE Access*, vol. 4, pp. 3999–4010, 2016.
[23] J. Lee, H. J. Lee, J.-Y. Kim, and I.-K. Cho, "Gaped two-loop antenna-based magnetic transceiver with an empirical model for wireless underground communication," *IEEE Access*, vol. 9, pp. 34962–34974, 2021.
[24] B. Gulbahar and O. B. Akan, "A communication theoretical modeling and analysis of underwater magneto-inductive wireless channels," *IEEE Trans. Wireless Commun.*, vol. 11, no. 9, pp. 3326–3334, Sep. 2012.
[25] M. C. Domingo, "Magnetic induction for underwater wireless communication networks," *IEEE Trans. Antennas Propag.*, vol. 60, no. 6, pp. 2929–2939, Jun. 2012.
[26] A. R. Silva and M. Moghaddam, "Operating frequency selection for low-power magnetic induction-based wireless underground sensor networks," in *Proc. IEEE Sensors Appl. Symp. (SAS)*, Apr. 2015, pp. 1–6.
[27] S. Kisseleff, I. F. Akyildiz, and W. H. Gerstacker, "Throughput of the magnetic induction based wireless underground sensor networks: Key optimization techniques," *IEEE Trans. Commun.*, vol. 62, no. 12, pp. 4426–4439, Dec. 2014.
[28] X. Tan, Z. Sun, P. Wang, and Y. Sun, "Environment-aware localization for wireless sensor networks using magnetic induction," *Ad Hoc Netw.*, vol. 98, Mar. 2020, Art. no. 102030.
[29] M. Hott, P. A. Hoeher, and S. F. Reinecke, "Magnetic communication using high-sensitivity magnetic field detectors," *Sensors*, vol. 19, no. 15, p. 3415, Aug. 2019.
[30] K. Kim, S. Ryu, J.-Y. Kim, I.-K. Cho, H.-J. Lee, J. Lee, and S. Ahn, "Giant magnetoimpedance receiver with a double-superheterodyne topology for magnetic communication," *IEEE Access*, vol. 9, pp. 82903–82908, 2021.
[31] A. Asfour, M. Zidi, and J. Yonnet, "High frequency amplitude detector for GMI magnetic sensors," *Sensors*, vol. 14, no. 12, pp. 24502–24522, 2014.
[32] D. A. Anderson, R. E. Sapiro, and G. Raithel, "An atomic receiver for AM and FM radio," *IEEE Trans. Antennas Propag.*, vol. 69, no. 5, pp. 2455–2462, Apr. 2020.
[33] J. H. Kim and D.-R. Son, "Construction of differential type search coil magnetometer," *J. Korean Magn. Soc.*, vol. 20, no. 5, pp. 178–181, Oct. 2010.
[34] B. Dziadak, A. Josko, and J. Starzynski, "Derivative differential, inductive sensors for short magnetic pulse measurements," in *Proc. 19th Int. Conf. Comput. Problems Electr. Eng.*, Sep. 2018, pp. 1–4.
[35] M. Saqib, S. N. Francis, and J. N. Francis, "Design and development of Helmholtz coils for magnetic field," in *Proc. Int. Youth Conf. Radio Electron., Electr. Power Eng. (REEPE)*, Mar. 2020, pp. 1–5.
[36] M. Cavaliere, O. McVeigh, H. A. Jaeger, S. Hinds, K. O'Donoghue, and P. Cantillon-Murphy, "Inductive sensor design for electromagnetic tracking in image guided interventions," *IEEE Sensors J.*, vol. 20, no. 15, pp. 8623–8630, Aug. 2020.
[37] *Part 11: Wireless LAN Medium Access Control (MAC) and Physical Layer (PHY) Specifications*, Standard 802.11ac, IEEE, 2013.
[38] R. C. Yob, N. Seman, and S. N. A. M. Ghazali, "Error vector magnitude analysis for wideband QPSK and QAM six-port modulator," in *Proc. IEEE Int. RF Microw. Conf.*, Dec. 2011, pp. 149–153.
[39] W. Zhang, A. Hasan, F. M. Ghannouchi, M. Helaoui, Y. Wu, L. Jiao, and Y. Liu, "Homodyne digitally assisted and spurious-free mixerless direct carrier modulator with high carrier leakage suppression," *IEEE Trans. Microw. Theory Techn.*, vol. 66, no. 3, pp. 1475–1488, Mar. 2018.

JANG-YEOL KIM received the B.S., M.S., and Ph.D. degrees in information and communication engineering from Chungbuk National University, Cheongju, Republic of Korea, in 2010, 2012, and 2017, respectively. Since 2012, he has been with the Electronics Telecommunications Research Institute, Daejeon, Republic of Korea. His research interests include antenna design, thermal therapy algorithms, microwave sensing, electromagnetic sensors, and magnetic transceiver systems.

HYUN JOON LEE received the B.S., M.S., and Ph.D. degrees from the Department of Physics, Pusan National University, Busan, South Korea, in 2008, 2011, and 2018, respectively. From 2018 to 2019, he was a Postdoctoral Associate at the Korea Research Institute of Standards and Science, working on optical magnetometry. Since 2019, he has been with the Electronics and Telecommunications Research Institute, Daejeon, South Korea. His research interests include ultra-low field magnetic resonance and the development of highly sensitive quantum sensors.

JAE-HO LEE was born in Daegu, South Korea, in March 1974. He received the B.S. degree in electronic and electrical engineering from Kyungpook National University, Daegu, in 2002, the M.S. degree in electrical and electronic engineering from the Korea Advanced Institute of Science and Technology (KAIST), Daejeon, South Korea, in 2004, and the Ph.D. degree in electrical and electronic engineering from the Tokyo Institute of Technology (TIT), Tokyo, Japan, in 2010. He received a Presidential Award for Leaders of the 21st Century from the Ministry of Education of Korea, in 2002. From 2004 to 2005, he worked on the Mobile Communication PM Team of the Institute of Information and Technology Assessment (IITA), Daejeon. He also worked with the Radar Research Center, Samsung Thales, Yongin, Gyeonggi-do, South Korea, from 2010 to 2012. From 2013 to 2022, he was a Principal Researcher at the Electronics and Telecommunications Research Institute (ETRI), South Korea. Since September 2022, he has been with Kunsan National University (KSNU), Gunsan, South Korea, where he is currently an Assistant Professor with the Department of Electronic Engineering. His research interests include waveguide slot arrays, millimeter wave antennas, radar systems, biomedical implantable devices, and magnetic communications.

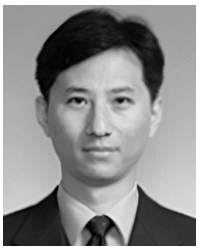

JUNG HOON OH received the B.S. degree in electronics from Kyungpook National University, Daegu, South Korea, in 1997, and the M.S. degree in electronic engineering from the Korea Advanced Institute of Science and Technology (KAIST), Daejeon, South Korea, in 1999. He is currently with the Electronics and Telecommunications Research Institute (ETRI), Daejeon. His research interests include magnetic field communication in extreme environments and atomic-based electric field measurement.

IN-KUI CHO received the B.S. and M.S. degrees from the Department of Electronic Engineering, Kyungpook National University, Daegu, South Korea, in 1997 and 1999, respectively, and the Ph.D. degree in electrical engineering from the Korean Advanced Institute of Science and Technology, Daejeon, South Korea, in 2007. Since May 1999, he has been with the Electronics and Telecommunications Research Institute, Daejeon, where he has designed and developed an optical backplane, optical chip-to-chip interconnect system, and magnetic resonance wireless power transfer. His current research interests include the simulation and development of WPT components and magnetic field communication, such as planar magnetic resonators, magnetic resonators for three-dimensional WPT and electromagnetic sensors, and magnetic transceiver systems.